Density Functional Theory studies of cluster states in nuclei

J.-P. Ebran,[1] E. Khan,[2] T. Nikšić,[3] and D. Vretenar[3]

[1]*CEA,DAM,DIF, F-91297 Arpajon, France*
[2]*Institut de Physique Nucléaire, Université Paris-Sud, IN2P3-CNRS, F-91406 Orsay Cedex, France*
[3]*Physics Department, Faculty of Science, University of Zagreb, 10000 Zagreb, Croatia*

(Dated: September 29, 2014)

The framework of nuclear energy density functionals is applied to a study of the formation and evolution of cluster states in nuclei. The relativistic functional DD-ME2 is used in triaxial and reflection-asymmetric relativistic Hartree-Bogoliubov calculations of relatively light $N = Z$ and neutron-rich nuclei. The role of deformation and degeneracy of single-nucleon states in the formation of clusters is analyzed, and interesting cluster structures are predicted in excited configurations of Be, C, O, Ne, Mg, Si, S, Ar and Ca $N = Z$ nuclei. Cluster phenomena in neutron-rich nuclei are discussed, and it is shown that in neutron-rich Be and C nuclei cluster states occur that are characterized by molecular bonding of α-particles by the excess neutrons.

PACS numbers: 21.60.Jz, 21.10.Gv, 27.20.+n, 27.30.+t

arXiv:1406.2473v2 [nucl-th] 26 Sep 2014

I. INTRODUCTION

Nuclear Energy Density Functional (EDF) provides a comprehensive and accurate description of ground-state properties and collective excitations over the whole nuclide chart. In the last decade EDFs have also been successfully applied to studies of clustering phenomena, and this framework enables a consistent microscopic analysis of the formation and evolution of cluster structures that is not limited to the lightest nuclei [1–9]. To describe the phenomenon of nuclear clustering already in the most basic EDF implementation, the self-consistent mean-field level, it is necessary to break as many spatial symmetries of the nuclear system as possible, and this implies a considerable computational cost. This explains the rather recent application of EDF-based methods to detailed quantitative studies of nuclear clustering. Consequently this approach provides a basis for the theoretical study of coexistence of cluster states and mean-field-type states. Cluster structures can, in fact, be considered as a transitional phase between the quantum liquid (nucleonic matter) phase and a crystal phase that does not occur in finite nuclei. Similar phase transition between the liquid and crystal phases are found in studies of mesoscopic systems such as quantum dots [10], or bosons in a rotating trap [11].

The solid (crystal) vs. quantum liquid nature of nuclear matter has been analyzed using the quantality parameter [12], defined as the ratio of the zero-point kinetic energy of the confined nucleon to its potential energy. The typical value obtained for nuclear matter is characteristic for a quantum liquid phase and reflects the well-known fact, recently confirmed by microscopic self-consistent Green's function calculation [13], that a nucleon in nuclear matter has a large mean-free path of 4 to 5 fm. The quantality parameter, however, is defined for infinite homogeneous systems and its applicability to finite nuclei is limited by the fact that it does not contain any nuclear mass or size dependence. Cluster states in finite nuclei introduce an additional phase of nucleonic matter, and to analyze localization and the phenomenon of clustering a quantity must be considered that is sensitive to the nucleon number and size of the nucleus. This is the localization parameter introduced in Refs. [4–6]. Its value increases with mass and describes the gradual transition from a hybrid phase in light nuclei, characterized by the spatial localization of individual nucleon states that leads to the formation of cluster structures, toward the Fermi liquid phase in heavier nuclei. The relationship between the quantality and the localization parameters is detailed in Appendix A.

In this work we apply nuclear EDF to a study of the formation and evolution of cluster states in nuclei. The framework of nuclear EDFs and the role of spatial localization of the individual single-nucleon states is reviewed in section II. Section III presents an analysis of the role of deformation and pronounced level degeneracy on the formation of clusters, and includes a number of examples of cluster structures in excited states. Cluster phenomena and molecular bond in neutron-rich nuclei are discussed in section IV, and section V contains a short summary and conclusion of the present study.

II. NUCLEAR ENERGY DENSITY FUNCTIONALS

The framework of EDFs provides a global approach to nuclear structure and enables an accurate description of ground-state properties and collective excitations over the whole chart of nuclides. At a moderate computational cost modern non-relativistic and relativistic EDFs can describe the evolution of structure phenomena from relatively light systems to superheavy nuclei, and from the valley of β-stability to the particle drip-lines.

The nuclear EDF is built from powers and gradients of ground-state nucleon densities and currents, representing distributions of matter, spins, momentum and kinetic energy. In principle a nuclear EDF can incorporate all short-range correlations related to the repulsive core of

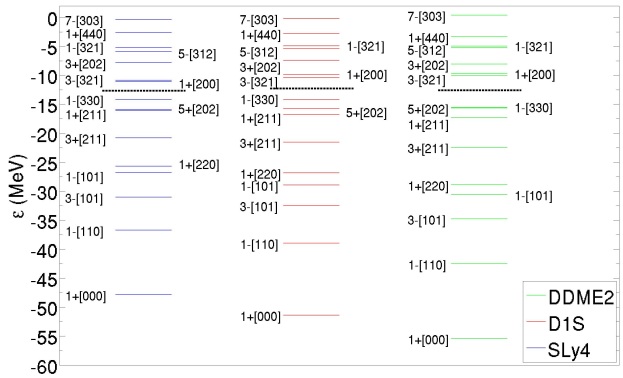

FIG. 1: (color online) Neutron single-particle levels of ^{36}Ar that correspond to the SCMF solutions calculated with the Skyrme functional SLy4, the Gogny effective interaction D1S, and the relativistic density functional DD-ME2. The levels are labelled by the Nilsson quantum numbers, and dotted lines denote the position of the Fermi level.

the inter-nucleon interaction, and long-range correlations mediated by nuclear resonance modes. An additional functional of the pairing density is included to account for effects of superfluidity in open-shell nuclei.

The ground-state energy and density of a given system can be determined by minimizing an EDF with respect to the 3-dimensional density. The self-consistent scheme introduces a local effective single-particle potential, such that the exact ground-state density of the interacting system of particles equals the ground-state density of the auxiliary non-interacting system, expressed in terms of the lowest occupied single-particle orbitals. The many-body dynamics is represented by independent nucleons moving in local self-consistent mean-field (SCMF) potentials that correspond to the actual density and current distributions of a given nucleus.

A broad range of nuclear structure phenomena have been analyzed using Skyrme, Gogny and relativistic EDFs [14–20]. These global functionals present different realizations of a universal nuclear EDF governed by the underlying theory of strong interactions. With relatively small sets of global parameters determined by empirical properties of nucleonic matter and data on finite nuclei, structure models based on Skyrme, Gogny or relativistic functionals provide a consistent description of a vast quantity of nuclear data. Even though results for ground-state observables (e.g. binding energies, charge radii) obtained with different functionals are rather similar and of comparable agreement with data, calculated quantities that are not directly observable can show marked differences. One such quantity is the auxiliary local SCMF potential. In Fig. 1 we plot the neutron single-particle levels of ^{36}Ar calculated with the Skyrme functional SLy4 [21], the Gogny effective interaction D1S [22, 23], and the relativistic density functional DD-ME2 [24]. The levels are labelled by the Nilsson quantum numbers, and correspond to ground-state SCMF solutions with the assumption of an axially symmetric quadrupole deformation. Dotted lines denote the position of the Fermi level. Even though all three functionals predict very similar ground-state properties (cf. also Fig. 2) and, therefore, similar ordering and density of levels close to the Fermi surface, the depths of the corresponding SCMF potentials are markedly different. The deepest potential correspond to the relativistic functional DD-ME2 (-82.4 MeV), whereas the potential of the Skyrme functional SLy4 is fairly shallow (-72.4 MeV). The position of the 1s state shows that the effective depth of the D1S potential lies between the ones of DD-ME2 and SLy4. One finds the same picture for the proton states except, of course, for the effect of Coulomb repulsion.

In Ref. [4] we found qualitatively the same difference for the SCMF potentials of ^{20}Ne calculated with SLy4 and DD-ME2. Even though the SCMF potential is not an observable, a deeper confining potential leads to a more pronounced localization of the single nucleon wave functions and enhances the probability of formation cluster structures in excited states close to the energy threshold for α-particle emission. The formation of nuclear clusters is similar to a transition from a superfluid to a Mott insulator phase in a gas of ultracold atoms held in a three-dimensional optical lattice potential [25, 26]. As the potential depth of the lattice is increased, a transition is observed from a phase in which each atom is spread out over the entire lattice, to the insulating phase in which atoms are localized with no phase coherence across the lattice. In the nuclear case one cannot, of course, vary the depth of the single-nucleon potential because the nucleus is a self-bound system. However, the same effect can be obtained by performing self-consistent calculations using different EDFs or effective interactions, as illustrated in Fig. 1 for SLy4, D1S and DD-ME2.

To investigate the role of deformation in the formation of clusters, we perform deformation-constrained SCMF calculations by imposing constraints on the mass multipole moments of a nucleus. The corresponding equations (Schrödinger-like for non-relativistic functionals, or Dirac-like for relativistic EDFs, with the Hamiltonian defined as the functional derivative of the corresponding EDF with respect to density) are solved in the intrinsic frame of reference attached to the nucleus, in which the shape of the nucleus can be arbitrarily deformed. In the present study we employ SCMF models that allow breaking both the axial and reflection symmetries [14]. As an illustration in Fig. 2 we display the binding energies of the self-conjugate nucleus ^{36}Ar as functions of the axial quadrupole deformation parameter β_2, calculated with SLy4 and D1S using the Hartree-Fock-Bogoliubov (HFB) model [23, 27], and with the functional DD-ME2 employing the relativistic Hartree-Bogoliubov (RHB) approach [18]. Pairing correlations are taken into account

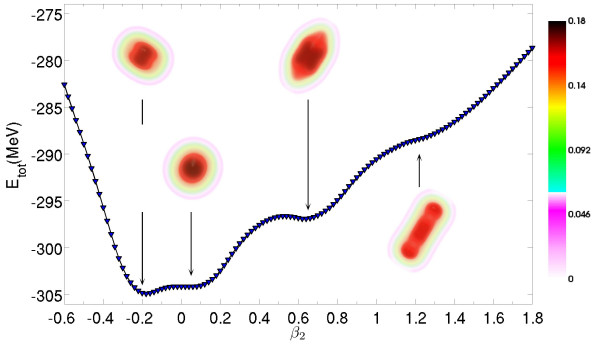

(a) SLy4

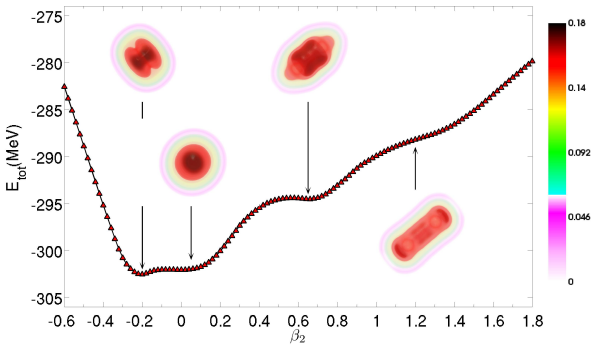

(b) D1S

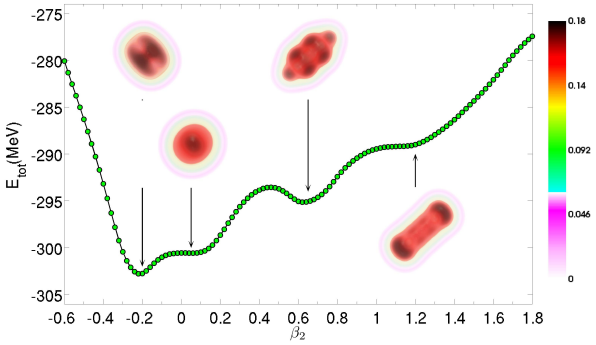

(c) DD-ME2

FIG. 2: (color online) Self-consistent binding energy curves of ^{36}Ar as functions of the quadrupole deformation parameter β_2, calculated with the functionals SLy4, D1S and DD-ME2. The insets display the corresponding intrinsic nucleon density distributions in the reference frame defined by the principal axes of the nucleus.

by a delta-pairing force for calculations with the Skyrme functional, whereas for the RHB calculations with DD-ME2 the pairing interaction is separable in momentum space, and determined by two parameters adjusted to reproduce the Gogny pairing gap in symmetric nuclear matter [28]. The curves of the total energy as a function of quadrupole deformation are obtained in a SCMF approach by imposing a constraint on the axial quadrupole moment. The parameter β_2 is directly proportional to the intrinsic mass quadrupole moment. For all three functionals the calculated equilibrium shape of ^{36}Ar is a slightly oblate, axially symmetric quadrupole ellipsoid with $\beta_2 \approx -0.2$. For the equilibrium deformation and few additional values of β_2, in the insets of Fig. 2 we also include the corresponding intrinsic nucleon density distributions in the reference frame defined by the principal axes of the nucleus. Here one already observes an interesting effect that was previously noted in our studies of Refs. [4–6], namely that deeper potentials lead to a more pronounced spatial localization of nucleonic densities. In general, we find that relativistic functionals, when compared to Skyrme and Gogny functionals, are characterized by deeper SCMF potentials. As noted in Ref. [4], the depth of a relativistic potential is determined by the difference between two large fields: an attractive (negative) Lorentz scalar potential of magnitude around 400 MeV, and a repulsive Lorentz vector potential of roughly 320 MeV (plus the repulsive Coulomb potential for protons). The sum of these potentials (about 700 MeV) determines the effective single-nucleon spin-orbit force in a unique way, whereas in a non-relativistic EDF framework the spin-orbit potential is included in a purely phenomenological way, with a strength parameter adjusted to empirical energy spacings between spin-orbit partner states. In the relativistic case the scalar and vector fields determine both the effective spin-orbit force and the SCMF potential, and the latter is generally found to be deeper than the non-relativistic mean-field potentials. In the following sections we, therefore, perform SCMF calculations based on the relativistic functional DD-ME2, which predicts equilibrium density distributions that are more localized, often with pronounced cluster structures.

III. DEFORMATIONS AND EXCITED CONFIGURATIONS

A unique feature of light nuclei is the coexistence of the nuclear mean-field and cluster structures, as expressed by the well-known Ikeda diagram [29–33]. A certain degree of localization of nucleonic densities is already present in mean-field ground-state configurations [4, 34, 35], and this facilitates the formation of cluster structures in excited states. Close to the particle emission threshold continuum effects become important for a quantitative description of nuclear clustering [36]. Deformation in light nuclei plays, of course, an important role in the formation of clusters [1, 2, 6, 31, 37]. The relationship between α-clusters and single-particle states in deformed nuclei has been extensively studied [31, 32, 38]. For instance, the Bayman-Bohr theorem [39] states that the SU(3) shell model wave function of a ground state is in most cases equivalent to the cluster Brink wave function in the limit when the inter-alpha distance vanishes. However, this

important link only relates a cluster wave function to a mean-field type one in this specific limit. The present EDF-based approach allows one to go a step further and establish a link between cluster states and the single-particle spectrum.

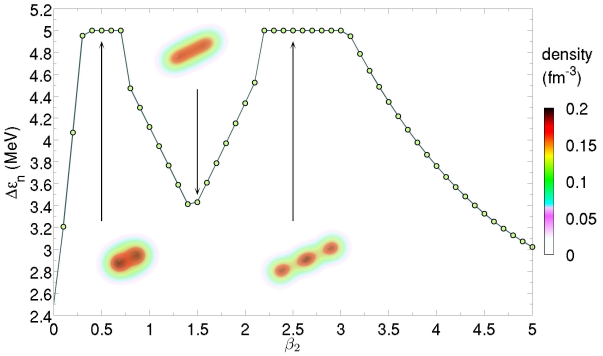

(a) ^{12}C

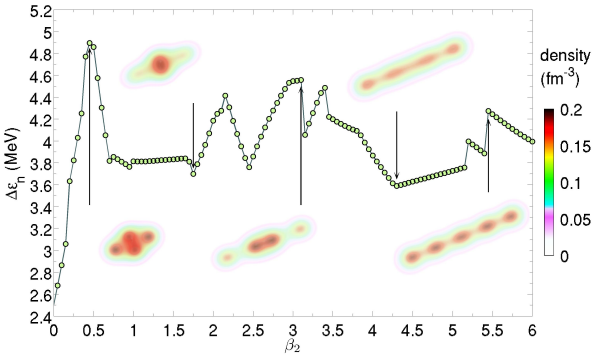

(b) ^{20}Ne

FIG. 3: (color online) Mean value of the energy gap between consecutive occupied neutron levels as a function of the axial quadrupole deformation parameter β_2 for ^{12}C (a) and ^{20}Ne (b). The insets display the total nucleonic density at the corresponding deformation. To limit the vertical scale the maximum mean value of the energy gap in the plot does not exceed 5 MeV.

A. Axially-symmetric quadrupole deformations

As stated by Rae [40], the degeneracy of single-nucleon states at a given deformation could generate clusters because of levels crossing. Here we analyze how degeneracy affects the formation of α clusters in self-conjugate nuclei. As noted by Aberg [38], an isolated level of the single-particle energy spectrum in a deformed self-conjugate $N = Z$ nucleus can correspond to an alpha-cluster, because of both time-invariance symmetry and isospin symmetry: two protons and two neutrons have similar wave functions, and the localization of these functions facilitates the formation of α-clusters. Hence, pronounced level degeneracy (or isolated levels in the case of alpha-clustering) allows to explain: i) why $N = Z$ and deformed nuclei favor cluster formation, ii) the link between the depth of the confining potential and cluster formation and, iii) why cluster structures mainly occur in light nuclei. The second point is related to the fact that pronounced degeneracy is driven by the depth of the potential [41], and this issue has already been analyzed in our previous studies [4–6]. The answer to the third question comes from the fact that level density is generally smaller in lighter nuclei and this favors the occurrence of isolated single-particle levels or degeneracy at certain deformations.

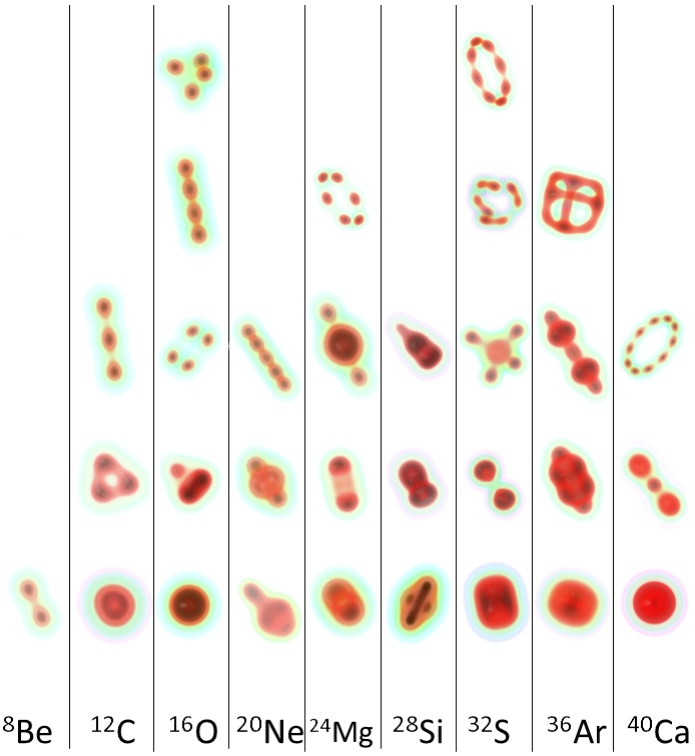

FIG. 4: (Color online) Positive-parity projected density plots obtained for a number of excited configurations in $N = Z$ nuclei. For each nucleus the density in the bottom row corresponds to the equilibrium configuration. Other selected densities are displayed in order of increasing excitation energy.

Let us illustrate this concept using the microscopic EDF framework with the examples of axially deformed quadrupole shapes of ^{12}C and ^{20}Ne. The self-consistent mean-field calculations with the relativistic functional DD-ME2 and a separable pairing interaction are performed using the implementation of the RHB model described in Ref. [42]. The RHB equations are solved in the configurational space of harmonic oscillator wave functions with appropriate symmetry, whereas the densities are computed in coordinate space. The method can be applied to spherical, axially and non-axially deformed nuclei. The map of the energy surface as a function of

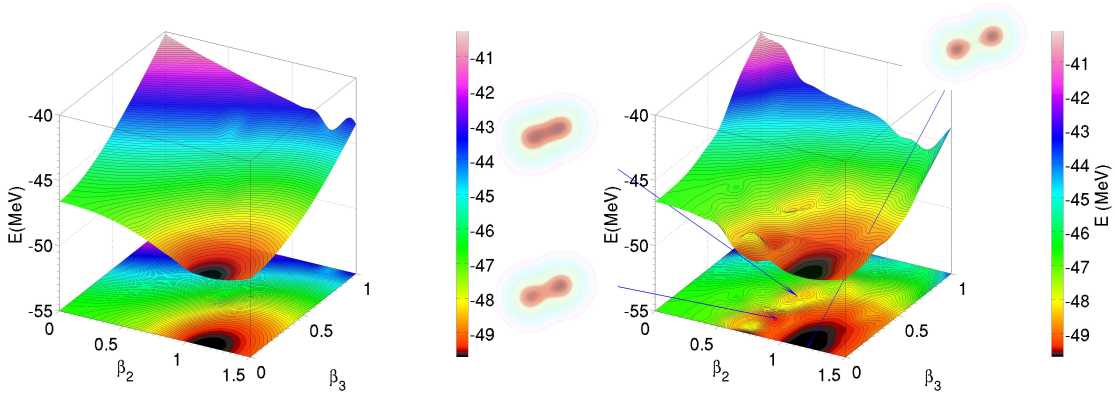

(a) ^{8}Be ($K = 0$) Mean-Field (b) ^{8}Be ($K^{\pi} = 0^{+}$) PAV

FIG. 5: (color online) Self-consistent energy surfaces of ^{8}Be, calculated with DD-ME2 by imposing constraints on both the axial quadrupole and octupole deformation parameters β_2 and β_3 (left), and the corresponding positive parity-projected energy surfaces (right).

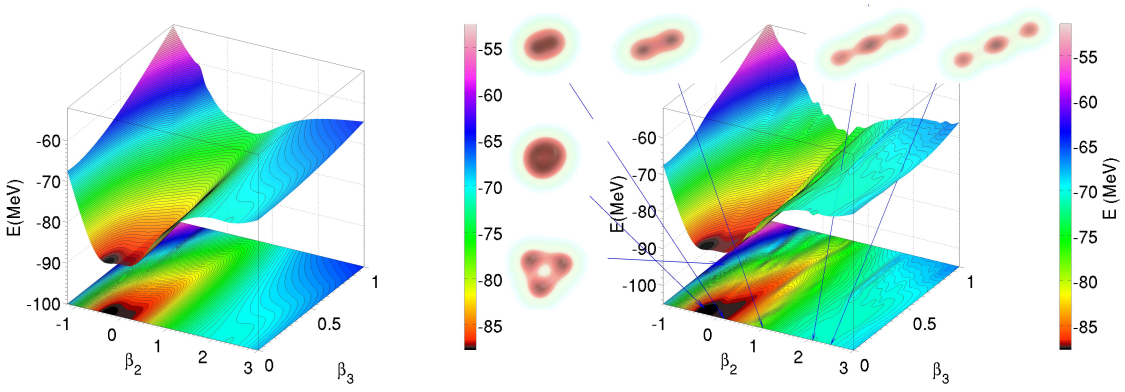

(a) ^{12}C ($K = 0$) Mean-Field (b) ^{12}C ($K^{\pi} = 0^{+}$) PAV

FIG. 6: (color online) Same as in the caption to Fig. 5 but for the isotopes ^{12}C.

quadrupole deformation parameters is obtained by solving the RHB equation with constraints on the axial and triaxial mass quadrupole moments of a given nucleus. The method of quadratic constraints uses an unrestricted variation of the function

$$\langle \hat{H} \rangle + \sum_{\mu=0,2} C_{2\mu}(\langle \hat{Q}_{2\mu} \rangle - q_{2\mu})^2, \quad (1)$$

where $\langle \hat{H} \rangle$ is the total energy and $\langle \hat{Q}_{2\mu} \rangle$ denotes the expectation value of the mass quadrupole operators

$$\hat{Q}_{20} = 2z^2 - x^2 - y^2 \quad \text{and} \quad \hat{Q}_{22} = x^2 - y^2. \quad (2)$$

$q_{2\mu}$ is the constrained value of the multipole moment and $C_{2\mu}$ the corresponding stiffness constant [41].

By increasing the prolate quadrupole deformation in the axially symmetric self-consistent calculation with the constraint on the axial quadrupole moment, ^{12}C and ^{20}Ne display a series of cluster configurations until eventually reaching the linear α-chain structure (Fig 3). To show the role of level degeneracy, Fig 3 displays the mean value of the energy gap between consecutive occupied neutron single-particle levels as a function of the deformation parameter β_2. The mean value of the energy gap is defined as

$$\Delta\epsilon_n \equiv < \Delta\epsilon_i > \quad (3)$$

where $\Delta\epsilon_i \equiv \epsilon_{i+1} - \epsilon_i$ is the energy gap between two successive neutron single-particles levels. At deformations for which the maximum mean value of the energy gap exceeds 5 MeV, we only plot this value so that the scale of the vertical axis does not become too large to display. A pronounced correlation between the enhancement of energy gaps between the single-particle levels and alpha-cluster formation can clearly be identified. Both for ^{12}C and ^{20}Ne the density profiles show more pronounced localization of α clusters at deformations at which the mean value of the energy gap between consecutive levels exhibits a sharp increase.

B. Quadrupole and octupole deformations and parity-projected energy surfaces

Recent cranking SCMF calculations of high-spin rotating nuclei produced interesting exotic cluster configurations such as, for instance, in ^{16}O and ^{40}Ca [1, 2, 43]. In the present study cluster shapes occur as local minima at large deformations on the $(\beta_2, \gamma, \beta_3, \beta_{32})$ energy hypersurface. As an illustration, Figure 4 displays a sample of various cluster shapes in self-conjugate nuclei, obtained in triaxial and reflection-asymmetric RHB calculations using the functional DD-ME2. For each of the nuclei shown in Fig. 4 densities that correspond to positive-parity projected intrinsic states are arranged in order of increasing energy. Most of them correspond to local minima on the deformation energy surface, except for the ring states. The bottom row displays the lowest energy (equilibrium) density distributions. This figure represents the microscopic EDF-based analogue of the original Ikeda diagram, which illustrates the coexistence of the nuclear mean-field and various cluster structures that appear close to the (multi) α-separation threshold energies [29]. For instance, already the equilibrium density of ^{8}Be displays a two-α cluster configuration [44–46]. In the case of ^{12}C, the equilibrium self-consistent mean-field configuration exhibits a slightly oblate triangular distribution of the three α particles (i.e. the axial octupole moment does not vanish in the equilibrium configuration), which becomes much more pronounced in the excited configuration shown in the second row, in agreement with very recent experimental results [47]. At still higher energies we find a linear chain configuration of the three α particles. ^{16}O displays the very interesting 4α cluster configuration with tetrahedral symmetry, a result very recently obtained using the constrained SCMF method [3, 6], the algebraic cluster model [48], and *ab initio* lattice calculations using chiral nuclear effective field theory [49]. For heavier $Z = N$ nuclei, in Fig. 4 we include a variety of exotic cluster configurations. For instance, as noted in the original Ikeda description [29], the lowest cluster configuration of ^{20}Ne corresponds to an $\alpha + {}^{16}$O core state.

In the next section we will consider, in particular, the occurrence of clusters in exotic Be and C isotopes. In the case of the N=Z nuclei, the axial quadrupole and octupole nucleonic density distributions of ^{8}Be and ^{12}C correspond to local minima on the energy surfaces as functions of axial quadrupole and octupole deformations displayed in Fig. 5 and Fig. 6, respectively. The self-consistent reflection-asymmetric axial energy surfaces are calculated by imposing constraints on both the axial quadrupole and octupole deformation parameters β_2 and β_3, respectively. In addition with the constraint on the moment associated to the octupole operator $\hat{Q}_3 = r^3 Y_{30}$, a constraint is also imposed on the center of mass of the nucleus: $\langle r^1 Y_{10} \rangle = 0$, to exclude the coupling to the spurious center of mass motion. The 3D energy maps and their projections on the $\beta_2 - \beta_3$ plane in the left part are obtained in SCMF calculations. The corresponding positive parity-projected energy surfaces are shown in the right part. Positive ($\pi = +1$) and negative ($\pi = -1$) parity-projected states are obtained by acting with the projector $\hat{\mathcal{P}}^\pi$ on the intrinsic state: $|\Phi^\pi(\beta_2, \beta_3)\rangle = \hat{\mathcal{P}}^\pi |\Phi(\beta_2, \beta_3)\rangle$, where

$$\hat{\mathcal{P}}^\pi = \frac{1}{2}\left(1 + \pi \hat{\Pi}\right). \quad (4)$$

The parity-projected energy surfaces are labelled with the deformation parameters of the intrinsic state and calculated using the relation [50]:

$$E_\pi(\beta_2,\beta_3) = \frac{\langle\Phi(\beta_2,\beta_3)|\hat{H}|\Phi(\beta_2,\beta_3)\rangle}{\langle\Phi(\beta_2,\beta_3)|\Phi(\beta_2,\beta_3)\rangle + \pi\langle\Phi(\beta_2,\beta_3)|\hat{\Pi}|\Phi(\beta_2,\beta_3)\rangle} + \pi\frac{\langle\Phi(\beta_2,\beta_3)|\hat{H}\hat{\Pi}|\Phi(\beta_2,\beta_3)\rangle}{\langle\Phi(\beta_2,\beta_3)|\Phi(\beta_2,\beta_3)\rangle + \pi\langle\Phi(\beta_2,\beta_3)|\hat{\Pi}|\Phi(\beta_2,\beta_3)\rangle} \quad (5)$$

For the equilibrium deformations and few additional local minima the nucleon density distributions in the reference frame defined by the principal axes of the nucleus are shown in the insets. The projected energy surface of ^{8}Be displays a deep minimum at very large quadrupole deformation that corresponds to a two-α configuration in agreement with a number of previous studies [44–46]. ^{12}C offers the possibility to investigate properties of three-center clusters. Linear chains of α-particles are predicted at very large prolate quadrupole deformations. A further possibility for three-center systems involves the formation of triangular shapes characterized by a discrete symmetry, and such structures are found in the region of oblate deformations (cf. also Ref. [47]).

IV. CLUSTER STRUCTURES IN NUCLEI FAR FROM STABILITY

Low-energy structures in a number of relatively light neutron-rich nuclei can be described by molecular bonding (π or σ) of α-particles by the excess neutrons [30, 31, 33, 51–56]. Figure 7 displays the total, proton and neutron axially symmetric intrinsic densities of Be isotopes in their equilibrium configurations, calculated using the RHB model with the DD-ME2 functional. One clearly notices the two-α structure, except in $^{10-13}$Be (the calculation for the odd-N isotopes is performed using the equal filling approximation), which display nearly spherical shapes because of the N=8 shell closure. Even though recent experimental studies of charge radii and the corresponding Fermionic Molecular Dynamics (FMD) calculations [57] indicate a pronounced quenching of the N=8 shell in ^{12}Be, a simple SCMF model based on a global functional that has not been specifically adjusted to this mass region, cannot produce such a structural change without additional adjustment of parameters and/or inclusion of correlations related to restoration of broken symmetries and configuration mixing.

To analyze the cluster content of Be isotopes, we investigate the partial densities that correspond to occupied single-particle states. Fig. 8 displays the total neutron distribution of ^{8}Be at equilibrium deformation, and details its decomposition into partial densities of each of the two occupied Nilsson states. A very similar picture is found for the proton density distributions. The partial densities provide a very clear picture of the formation of the two α clusters that appear in the total density distribution.

In the case of the neutron-rich Be isotopes, decomposing the total density into the $\alpha+\alpha$ structure and the density of the additional valence neutrons, a picture of nuclear molecular states emerges. A negative-parity orbital perpendicular to the $\alpha+\alpha$ direction is called a π-orbital, and a positive-parity orbital parallel to the $\alpha+\alpha$ direction is called a σ-orbital (cf. Fig. 7 of Ref. [58]). As an example here we consider ^{10}Be and ^{14}Be. The valence neutrons stabilize the two-center cluster structure of the $\alpha+\alpha$ core with π-like and σ-like molecular bonds (Figs. 9 and 10). The results obtained in the present calculation are consistent with predictions of the Antisymmetrized Molecular Dynamics model (cf. Ref. [58] and references cited therein), that is, the valence neutrons form a π-bond in the equilibrium state and a σ-bond in the excited state shown in Fig. 9. In the case of the more neutron-rich nucleus ^{14}Be, as shown in Fig. 10, already in the equilibrium state the valence neutrons form both π and

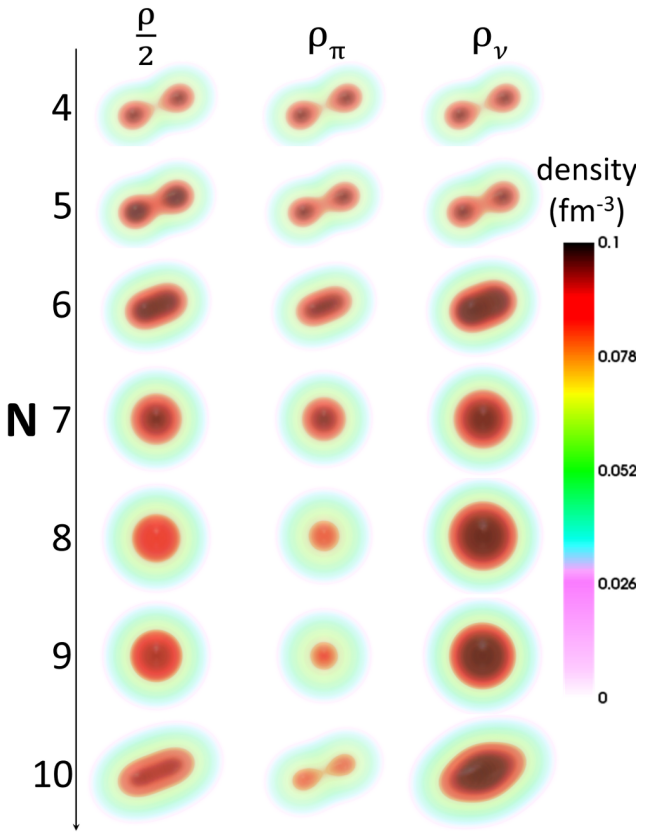

FIG. 7: (Color online) Total, proton and neutron SCMF equilibrium intrinsic densities for beryllium isotopes, calculated using the RHB model with the functional DD-ME2.

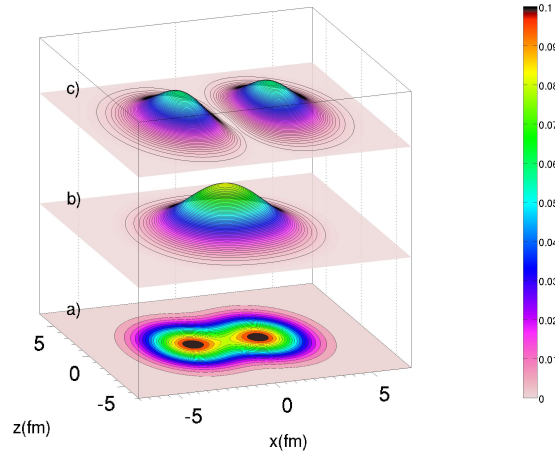

FIG. 8: (Color online) Contour plot of the ^{8}Be neutron density (a), and surface plots of the partial densities of each of the two occupied Nilsson states in the (Oxz) plane (b) and (c)).

σ bonds, similar to the results reported in Ref. [58].

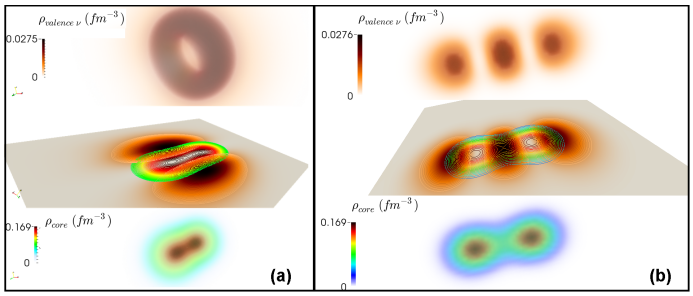

FIG. 9: (Color online) Intrinsic densities of ^{10}Be at equilibrium deformation (a), and for an excited configuration (b). From bottom to top: 3D density of the $\alpha+\alpha$ core; contour plots of the core density and the density of the valence neutrons in the (Oxz) plane; 3D density of the valence neutrons.

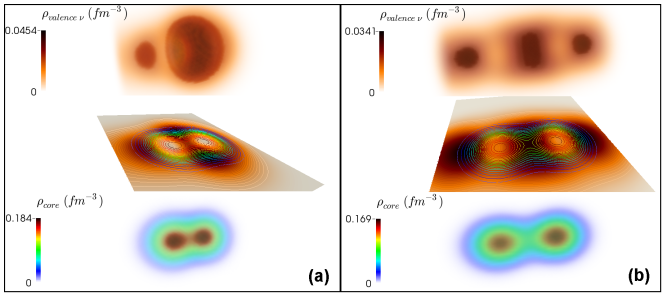

FIG. 10: (Color online) Same as in the caption to Fig. 9 but for the equilibrium deformation and an excited configuration of ^{14}Be.

An interesting topic is the occurrence of clusters in excited states of neutron-rich carbon isotopes [31]. In particular, the molecular-orbital structure in neutron-rich C isotopes was investigated using a microscopic molecular-orbit (MO) $\alpha+\alpha+\alpha+n+n+\ldots$ model [59], and it was shown that valence neutrons which occupy the π-orbit increase the binding energy and stabilize the linear chain of 3 α against the breathing-like breakup. However, when considering ^{12}C, ^{14}C, and ^{16}C, it was found that the linear-chain structure of ^{16}C ($(3/2^-_\pi)^2(1/2^-_\sigma)^2$) is the only one to be simultaneously stable against the breathing-like breakup and the bending-like breakup. Figs. 11 and 12 display the excess-neutron molecular orbits in excited configurations of ^{14}C and ^{16}C, calculated using the present EDF-based self-consistent microscopic approach. The decomposition of the density of an excited configuration of ^{14}C in terms of the 3 α core and the two valence neutrons is shown in Fig 11. We note that in this case correlations between the valence neutrons tend to favor a reflection asymmetric chain configuration. Accordingly, the intrinsic reflection-asymmetric chain configuration $\alpha-2n-\alpha-\alpha$, with the two valence neutrons forming a π-bond between the two α, is found at lower energy with respect to the reflection symmetric chain $\alpha-n-\alpha-n-\alpha$. A reflection-symmetric configuration with four valence neutrons, that is, $\alpha-2n-\alpha-2n-\alpha$ is favored in ^{16}C, as shown Fig 12 and similar to the results obtained with the AMD approach [31].

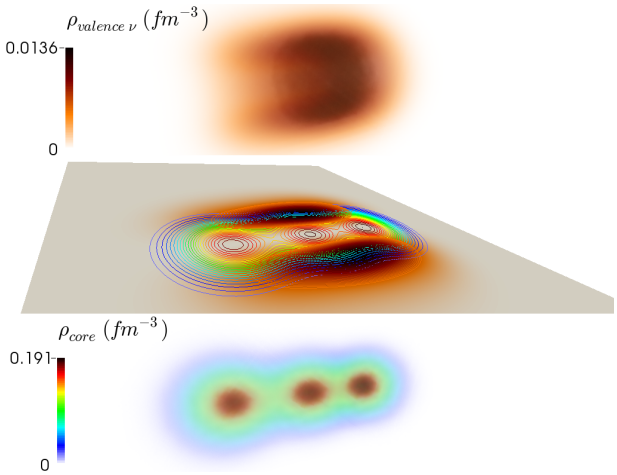

FIG. 11: (Color online) Nucleonic densities for an excited configuration of ^{14}C. From bottom to top: 3D density of the $\alpha+\alpha+\alpha$ core; contour plots of the core density and the density of the valence neutrons in the (Oxz) plane; 3D density of the valence neutrons.

On the proton-rich side a particularly interesting case is ^{10}C, which may be described as an $\alpha+\alpha+p+p$ structure. The unique feature of this system is that the removal of any one of the four constituents results in an unbound three-body system. It can, therefore, be considered as a super-Borromean or fourth-order Brunnian nuclear system [60, 61]. As the mirror nucleus of ^{10}Be, ^{10}C is expected to display a covalent 2-center chain configura-

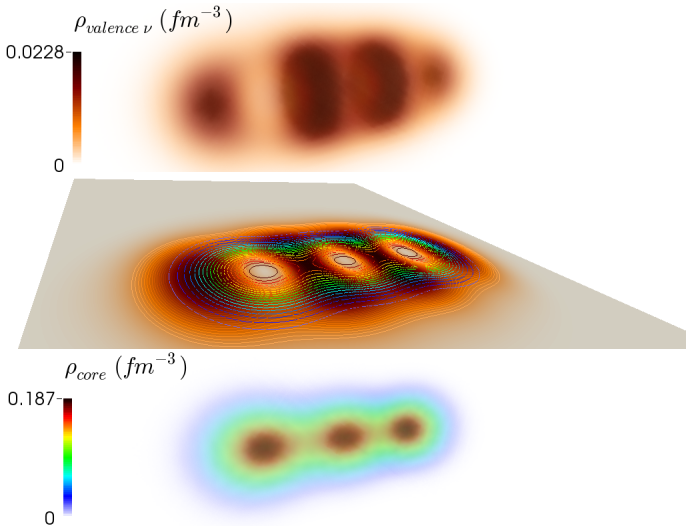

FIG. 12: (Color online) Same as in the caption to Fig. 11 but for an excited configuration of ^{16}C.

tion with a pair of protons as the covalent bond. Fig. 13 illustrates the results of our EDF-based self-consistent calculation for an excited configuration of ^{10}C, for which the two valence protons provide the molecular bonding for the $\alpha + \alpha$ core.

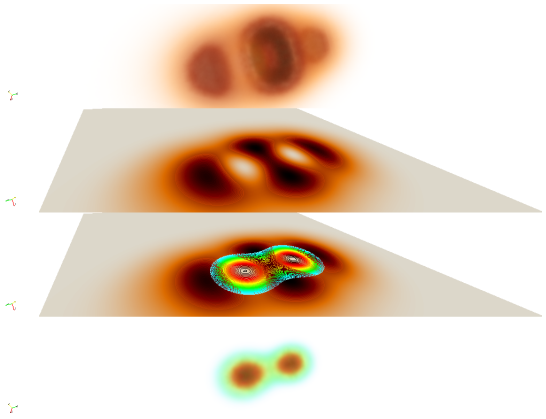

FIG. 13: (Color online) Nucleonic densities for an excited configuration of ^{10}C. From bottom to top: 3D density of the $\alpha + \alpha$ core; contour plots of the core density and the density of the valence protons in the (Oxz) plane; 3D density of the valence protons.

V. CONCLUSION

The formation of cluster states in nuclei has been investigated employing a theoretical framework based on nuclear EDF. By performing deformation constrained self-consistent Hartree-Fock-Bogoliubov (HFB) calculations with Skyrme and Gogny functionals, and relativistic Hartree-Bogoliubov (RHB) calculations with the functional DD-ME2, it has been shown that a deeper mean-field confining potential leads to a more pronounced localization of the single nucleon wave functions and enhances the probability of formation cluster structures in excited states. In particular, since the relativistic functional DD-ME2 produces the deepest potential among the considered functionals, we have used DD-ME2 in a series of axially-symmetric quadrupole and octupole constrained RHB calculations of relatively light $N = Z$, as well as neutron-rich nuclei. The role of deformation and degeneracy of single-nucleon states in the formation of clusters has been analyzed in detail, and a number of interesting cluster structures have been predicted in excited configurations that correspond to local minima on the parity-projected energy maps as functions of the quadrupole and octupole deformation parameters.

A particularly interesting topic is the occurrence of cluster configurations in neutron-rich nuclei. We have shown that in neutron-rich Be and C nuclei cluster states occur as a result of molecular bond (π or σ) of α-particles by the excess neutrons, and also that proton covalent bond can occur in ^{10}C.

Results obtained in this study demonstrate the feasibility of using nuclear EDF to explore the occurrence and evolution of α-cluster structures in relatively light $N = Z$ and neutron-rich nuclei. When compared to dedicated cluster models, this framework allows for a microscopic description of the coexistence of cluster states and mean-field-type states at low energies. The SCMF approach does not assume any constraint on the nucleonic wave function nor the existence of nucleon cluster structures, rather energy density functionals implicitly include many-body correlations that enable the formation of cluster states starting from microscopic single-nucleon degrees of freedom. For a quantitative description of cluster states, however, EDF-based structure models have to be developed that go beyond the static mean-field approximation, and include collective correlations related to the restoration of symmetries broken at the mean-field level, and to fluctuations of collective variables. These models can then be employed in analyses of cluster phenomena related to shell evolution and shape transitions, including detailed predictions of excitation spectra and electromagnetic transition rates.

Acknowledgement

This work was supported by the Institut Universitaire de France. The authors thank Peter Schuck and Matko Milin for reading the manuscript, many valuable discussions and suggestions.

Appendix A: The localization and quantality parameters

The localization parameter is used to characterize clusters as hybrid states between the crystal and quantum liquid phases in nuclei [4–6], whereas the quantality parameter describes the quantum liquid vs. crystal behavior of homogeneous nucleonic matter [12] and is defined by the relation:

$$\Lambda \hat{=} \frac{\hbar^2}{m r_0^2 V_0'} \tag{A1}$$

where r_0 is the typical inter-nucleon distance and V'$_0$ the characteristic magnitude of the inter-particle interaction (V'$_0$ $\simeq$100 MeV in the case of the nucleon-nucleon interaction). As discussed by Mottelson, the quantum liquid phase is obtained for $\Lambda > 0.1$, whereas the crystal phase is characterized by values of $\Lambda < 0.1$. Nuclei, of course, are in the quantum liquid phase. However, the quantality parameter Eq. (A1) depends on the nucleon-nucleon interaction only, and does not take into account the finite size effects at work in nuclei. Hence the localization parameter is defined as [4–6]

$$\alpha \hat{=} \frac{b}{r_0} = \frac{\sqrt{\hbar} A^{1/6}}{(2 m V_0 r_0^2)^{1/4}} \tag{A2}$$

where b is the typical dispersion of the single-nucleon wave function, and V_0 is the depth of the confining potential (V_0 $\simeq$75 MeV in the case of the nuclear mean-field [4]). One can therefore use α to analyze the evolution of nuclear configurations with respect to the number of constituents A [5, 6] and, in particular, systems where finite-size effects are relevant ($A < 10^3$). The crystal, cluster and liquid phases then correspond to $\alpha < 1$, $\alpha \sim 1$, and $\alpha > 1$, respectively.

In order to relate the quantality and localization parameters, we need to link the depth of the mean-field potential V_0 to the magnitude of the nucleon-nucleon interaction V_0'. Considering a short range n-n interaction $V_2(\vec{r}, \vec{r'})$ that can qualitatively be described by a hard core for r<r_0 and an attractive part of magnitude $-V_0'$ in the region between r_0 and r_0+a (Fig. 14):

$$V_2(\vec{r}, \vec{r'}) = V_2(R) = -V_0' \tag{A3}$$

for R between r_0 and r_0+a, with $R \equiv |\vec{r} - \vec{r'}|$.

The n-n interaction can also be approximated by

$$V_2(\vec{r}, \vec{r'}) = -V_0'' \delta(\vec{r} - \vec{r'} - \vec{r_0}) = -V_0'' \delta(\vec{R} - \vec{r_0}) \; . \tag{A4}$$

This can be justified by the short range-approximation of the nucleon-nucleon interaction, and such a zero-range approximation is successfully used, for instance, in Skyrme functionals. To be compatible with Eq. (A3), a<r_0.

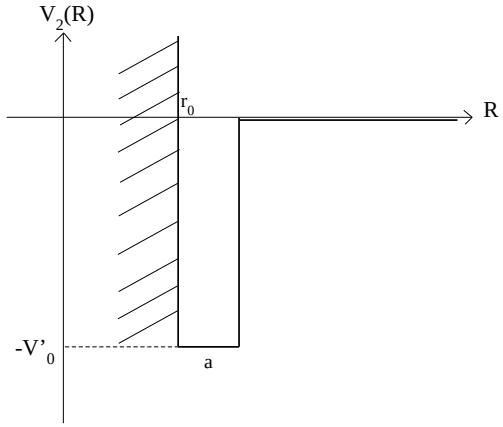

FIG. 14: Simple approximation of the n-n potential used to derive the relation between the localization and quantality parameters Eq. (A11).

The confining potential V(r) is, to a good approximation, the mean value of the n-n interaction over the nucleonic density [41]:

$$V(\vec{r}) \simeq \int V_2(\vec{r}, \vec{r'}) \rho(\vec{r'}) d\vec{r'} = -V_0'' \rho(\vec{r} - \vec{r_0}) \tag{A5}$$

Eq. (A5) expresses the fact that in a saturated system characterized by a short-range interaction, the mean-field potential displays a spatial dependence that corresponds to the shape of the density. From Eq. (A5) the depth of the mean-field potential is:

$$V_0 \approx V_0'' \rho_0 \tag{A6}$$

where $\rho_0 = 3/(4\pi r_0^3)$. Moreover, Eq. (A3) and (A4) yield

$$\int V_2(R) d\vec{R} = -V_0'' = -4\pi V_0' \int_{r_0}^{r_0+a} R^2 dR \; , \tag{A7}$$

and thus

$$V_0'' = \frac{4}{3} \pi V_0' \left[(r_0 + a)^3 - r_0^3 \right] \; . \tag{A8}$$

Inserting Eq. (A8) in (A6), one finally obtains

$$V_0 = \gamma V_0' \tag{A9}$$

with

$$\gamma \equiv \left[\left(1 + \frac{a}{r_0} \right)^3 - 1 \right] \; . \tag{A10}$$

Therefore, the relation between the depth of the mean-field potential V_0 and the magnitude of the n-n interaction V'$_0$ is linear and only depends, in this simple approximation, on the ratio a/r_0, that is, the width of the attractive part of the n-n interaction over the equilibrium distance between the nucleons. In finite nuclei, for typical

values of r_0 and a one gets $\gamma \simeq 3/4$. This is in agreement with the empirical values V_0=75 MeV and V'_0=100 MeV [12, 62]. Inserting now Eq. (A1) into Eq. (A2), and using Eq. (A9) with $\gamma = 3/4$, one finds the relation between the localization and quantality parameters

$$\alpha \simeq A^{1/6}\Lambda^{1/4} \,. \tag{A11}$$

[1] T. Ichikawa, J.A. Maruhn, N. Itagaki and S. Ohkubo, Phys. Rev. Lett. 107, 112501 (2011).
[2] T. Ichikawa, J.A. Maruhn, N. Itagaki, K. Matsuyanagi, P.-G. Reinhard, and S. Ohkubo, Phys. Rev. Lett. 109, 232503 (2012).
[3] M. Girod and P. Schuck, Phys. Rev. Lett. 111, 132503 (2013).
[4] J.P. Ebran, E. Khan, T. Nikšić and D.Vretenar, Nature 487, 341 (2012).
[5] J.P. Ebran, E. Khan, T. Nikšić and D. Vretenar, Phys. Rev. C 87, 044307 (2013).
[6] J.P. Ebran, E. Khan, T. Nikšić and D. Vretenar, Phys. Rev. C 89, 031303(R) (2014).
[7] J.A. Maruhn, M. Kimura, S. Schramm, P.-G. Reinhard, H. Horiuchi and A. Tohsaki, Phys. Rev. C 74, 044311 (2006).
[8] P. Arumugam, B.K. Sharma, S. K. Patra and Raj K. Gupta, Phys. Rev. C 71, 064308 (2005).
[9] J.M. Yao, N. Itagaki, and J. Meng, Arxiv1403:7940.
[10] H. Falakshahi and X. Waintal, Phys. Rev. Lett. 94, 046801 (2005).
[11] C. Yannouleas and U. Landman, Rep. Prog. Phys. 70 (2007) 2067
[12] B. Mottelson, Nuclear Structure, Les Houches, Session LXVI, 25 (1996).
[13] A. Rios and V. Somà, Phys. Rev. Lett. 108, 012501 (2012).
[14] M. Bender, P.H. Heenen, P.G. Reinhard, Rev. Mod. Phys. 75, 121 (2003).
[15] G.A. Lalazissis, P. Ring, D. Vretenar, *Extended Density Functionals in Nuclear Structure Physics* (Lecture Notes in Physics 641, Springer, 2004).
[16] J. Stone, P.G. Reinhard, Prog. Part. Nucl. Phys. 58, 587 (2007).
[17] J. Erler, P. Klüpfel, P.G. Reinhard, J. Phys. G 38, 033101 (2011).
[18] D. Vretenar, A.V. Afanasjev, G. Lalazissis, P. Ring, Phys. Rep. 409, 101 (2005).
[19] J. Meng, H. Toki, S. Zhou, S. Zhang, W. Long, Prog. Part. Nucl. Phys. 57, 470 (2006).
[20] T. Nikšić, D. Vretenar, P. Ring, Prog. Part. Nucl. Phys. 66, 519 (2011).
[21] E. Chabanat, P. Bonche, P. Haensel, J. Meyer, R. Schaeffer, Nucl. Phys. A 635, 231-256 (1998).
[22] J. F. Berger, M. Girod, and D. Gogny, Nucl. Phys. A 428, 23c (1984).
[23] J. F. Berger, M. Girod, and D. Gogny, Comp. Phys. Comm. 63, 365 (1991).
[24] G.A. Lalazissis, T. Niksic, D. Vretenar, P. Ring, Phys. Rev. C 71, 024312 (2005).
[25] M. Greiner, O. Mandel, T. Esslinger, T.W. Hänsch and I. Bloch, Nature 415, 39 (2002).
[26] D. Jaksch, C. Bruder, J. I. Cirac, C. W. Gardiner, and P. Zoller, Phys. Rev. Lett. 81, 3108 (1998).
[27] M.V. Stoitsov, J. Dobaczewski, W. Nazarewicz, P. Ring, Comp. Phys. Comm. 167, 43-63 (2005).
[28] T. Gonzales-Llarena, J.L. Egido, G.A. Lalazissis, P. Ring, Phys. Lett. B, 379, 13 (1996).
[29] K. Ikeda, N. Takigawa and H. Horiuchi, Prog. Theor. Phys. Suppl. 464 (1968).
[30] W.v Oertzen, M. Freer, Y. Kanada-En'yo, Phys. Rep. 432, 43 (2006).
[31] Y. Kanada En'yo, H. Horiuchi, Prog. Theor. Phys. Suppl. 142, 205 (2001).
[32] H. Horiuchi, Lecture Notes in Physics 818, 57 (2011).
[33] H. Horiuchi, K. Ikeda, and K. Kato, Prog. Theor. Phys. Suppl. 192, 1 (2012).
[34] P.-G. Reinhard, J.A. Maruhn, A.S. Umar, V.E. Oberacker, Phys. Rev. C 83, 034312 (2011).
[35] Bo Zhou, Zhongzhou Ren, Chang Xu, Y. Funaki, T. Yamada, A. Tohsaki, H. Horiuchi, P. Schuck, and G. Röpke, Phys. Rev. C86, 014301 (2012).
[36] J. Okolowicz, M. Ploszajczak, W. Nazarewicz, Prog. Theor. Phys. Suppl. 196, 230 (2012).
[37] L.M. Robledo, G.F. Bertsch, Phys. Rev. C 84, 054302 (2011).
[38] S. Aberg, L.-O. Jönsson, Z. Phys. A 349, 205 (1994).
[39] B.F. Bayman, A. Bohr, Nucl. Phys. 9, 956 (1958).
[40] W.D.M. Rae, Proc of the 5th Int. Conf. on clustering aspects in nuclear and subnuclear systems, Kyoto, Japan, Phys. Society of Japan, 80 (1989).
[41] P. Ring, P. Schuck, The Nuclear Many-Body Problem, Springer-Verlag, Heidelberg, (1980).
[42] T. Nikšić, N. Paar, D. Vretenar, and P. Ring, Prog. Comp. Phys. Comm. 185, 1808 (2014).
[43] Y. Funaki, M. Girod, H. Horiuchi, G. Röpke, P. Schuck, A. Tohsaki and T. Yamada, J. Phys. G 37, 064012 (2010).
[44] D.M. Brink, Proceedings of the International School of Physics Enrico Fermi, Academic Press, New York, 36, 247 (1966).
[45] A. Tohsaki, H. Horiuchi, P. Schuck, and G. Röpke, Phys. Rev. Lett. 87, 192501 (2001).
[46] R.B. Wiringa, S.C. Pieper, J. Carlson and V.R. Pandharipande, Phys. Rev. C62, 014001 (2000).
[47] D.J. Marín-Lámbarri, R. Bijker, M. Freer, M. Gai, Tz. Kokalova, D.J. Parker, and C. Wheldon, Phys. Rev. Lett. 113, 012502 (2014).
[48] R. Bijker and F. Iachello, Phys. Rev. Lett. 112, 152501 (2014).
[49] Evgeny Epelbaum, Hermann Krebs, Timo A. Lahde, Dean Lee, Ulf-G. Meissner, and Gautam Rupak, Phys. Rev. Lett. 112, 102501 (2014).
[50] L. M. Robledo, Int. J. Mod. Phys. E16, 337 (2007).
[51] W. von Oertzen, Z. Phys. A 354, 37 (1996); 357, 355 (1997).
[52] W. von Oertzen, Eur. Phys. J. A 11, 403 (2001).
[53] M. Freer, E. Casarejos, L. Achouri, C. Angulo, N.I. Ashwood, N. Curtis, P. Demaret, C. Harlin, B. Laurent, M. Milin, N.A. Orr, D. Price, R. Raabe, N. Soić, and V.A. Ziman, Phys. Rev. Lett. 96, 042501 (2006).

[54] M. Milin et al., Nucl. Phys. A 753, 263 (2005).
[55] P. Descouvemont and D. Baye, Phys. Lett. B 505, 71 (2001)
[56] M. Ito, N. Itagaki, and K. Ikeda, Phys. Rev. C 85, 014302 (2012)
[57] A. Krieger, K. Blaum, M.L. Bissell, N. Frömmgen, Ch. Geppert, M. Hammen, K. Kreim, M. Kowalska, J. Krämer, T. Neff, R. Neugart, G. Neyens, W. Nörtershäuser, Ch. Novotny, R. Sánchez, and D. T. Yordanov, Phys. Rev. Lett. 108, 142501 (2012).
[58] Y. Kanada-En'yo, Phys. Rev. C 85, 044320 (2012).
[59] N. Itagaki, S. Okabe, K. Ikeda, and I. Tanihata, Phys. Rev. C 64, 014301 (2001).
[60] R.J. Charity, K. Mercurio, L.G. Sobotka, J.M. Elson, M. Famiano, A. Banu, C. Fu, L. Trache, and R. E. Tribble, Phys. Rev. C 75, 051304(R) (2007).
[61] N. Curtis, N.L. Achouri, N.I. Ashwood, H.G. Bohlen, W.N. Catford, N.M. Clarke, M. Freer, P.J. Haigh, B. Laurent, N.A. Orr, N.P. Patterson, N. Soić, J.S. Thomas and V. Ziman, Phys. Rev. C 77, 021301 (2008); Phys. Rev. C 82, 029907(E) (2010).
[62] A.N. James, P.T. Andrews, P. Kirkby, B.G. Lowe, Nucl. Phys. A138, 145 (1969).